Design, fabrication, and low-power rf measurement of an *X*-band dielectric-loaded accelerating structure

Yelong Wei[1,6,7,*] Hikmet Bursali[1,2] Alexej Grudiev,[1] Ben Freemire,[3] Chunguang Jing,[3,4]
Rolf Wegner,[1] Joel Sauza Bedolla,[5] and Carsten Welsch[6,7]

[1]*CERN, Geneva CH-1211, Switzerland*
[2]*Sapienza University of Rome, Rome 00185, Italy*
[3]*Euclid Techlabs LLC, Bolingbrook, Illinois 60440, USA*
[4]*High Energy Physics Division, Argonne National Laboratory, Lemont, Illinois 60439, USA*
[5]*Lancaster University, Lancaster LA1 4YW, United Kingdom*
[6]*University of Liverpool, Liverpool L69 7ZX, United Kingdom*
[7]*Cockcroft Institute, Warrington WA4 4AD, United Kingdom*

This paper presents the design, fabrication, and low-power rf measurement of an externally powered *X*-band dielectric-loaded accelerating (DLA) structure with a dielectric constant $\varepsilon_r = 16.66$ and a loss tangent $\tan\delta = 3.43 \times 10^{-5}$. A dielectric matching section for coupling the rf power from a circular waveguide to an *X*-band DLA structure consists of a compact dielectric disk with a width of 2.035 mm and a tilt angle of 60°, resulting in a broadband coupling at a low rf field which has the potential to survive in the high-power environment. Based on simulation studies, a prototype of the DLA structure was fabricated. Results from low-power rf measurements and the comparison with simulated values are presented. A significant discrepancy was found between measurements and simulations. The detailed analysis on the fabrication errors which may cause the discrepancy is also discussed.

I. INTRODUCTION

Over the past few decades, there has been a major effort to understand the high gradient limits of disk-loaded metal accelerating structures [1–5], as well as to develop alternative structures that may be capable of producing high gradient [6–10]. One promising concept is the dielectric-loaded accelerating (DLA) structures which utilize dielectrics to slow down the phase velocity of traveling waves in the vacuum channel. A DLA structure comprises a simple geometry where a dielectric tube is surrounded by a conducting cylinder. Because of its simplicity, the DLA structure can be easily scaled from microwave frequency to THz regime. Simulation studies [11] have shown that the ratio of the peak electric field to the average accelerating field in a DLA structure is about unity, indicating that the accelerating gradient achieved is potentially higher than that of disk-loaded copper structures assuming dielectrics and metals have the similar breakdown limit. Moreover, the

relatively small diameter of DLA structures facilitates the use of quadrupole lenses around the structures. The DLAs are also advantageous in terms of the ease of applying damping schemes for beam-induced deflection modes [12–13], which can cause bunch-to-bunch beam breakup and intrabunch head-tail instabilities [14].

The DLA structures were initially proposed in the 1940s [15–18], and experimentally demonstrated in the 1950s [19–21]. Since that time, disk-loaded metallic structures have prevailed for accelerator research and development because of their high quality factor and high field holding capability. Thanks to remarkable progress in new ceramic materials with high dielectric permittivity ($\varepsilon_r > 20$), low loss ($\tan\delta \leq 10^{-4}$) [22–24], and ultralow-loss ($\tan\delta \leq 10^{-5}$) [25–26], studies on DLA structures are gradually being revived. For example, fused silica, chemical vapor deposition (CVD) diamond, alumina and other ceramics have been proposed as materials for DLA structures [27–29], and experimentally tested with high-power wakefield accelerating structures at Argonne National Laboratory [30–31]. In the past two decades, different kinds of DLA structures with improved performance have been reported, such as a hybrid dielectric and iris-loaded accelerating structure [32] reducing the ratio of the peak electric field to the average accelerating field to near unity, a dual-layered dielectric structure [33] and a multilayered dielectric structure [34] achieving a small rf power

*yelong.wei@cern.ch

attenuation, a disk-and-ring tapered accelerating structure [35] enabling a wide range of phase velocities, a dielectric disk accelerating structure [36] and a dielectric assist accelerating structure [37–40] realizing a high rf to beam efficiency.

There are several practical issues limiting the performance of DLA structures, such as surface multipactor [41–46] and breakdown [42]. The surface resonant multipactor has been always observed in experimental studies to absorb a large fraction of the incident rf power, which is identified as a problem limiting the gradient in DLA structures. An effective approach which uses an applied axial magnetic field to completely suppress this multipactor in DLA structures has been proposed [44] and demonstrated [45–46] in high-power experimental studies. In dielectric breakdown studies, a dielectric surface field breakdown threshold of 13.8 GV/m has been observed at THz frequencies [47]. Although there are few direct breakdown studies for externally powered DLA structures, no breakdown has been observed in several high-power tests carried out on a DLA structure at a level >5 MW [42–43,45–46]. It was also found that an rf coupling scheme is of particular importance to enable efficient coupling power into a DLA structure without breakdown. A scheme [48] using a combination of a side coupling slot and a tapered dielectric layer near the slot was proposed to couple the rf power from a rectangular waveguide into the DLA structure. The tapered dielectric matching section is a part of the DLA structure. However, breakdown was observed for such an rf coupler in the high-power test because of the strong electric field enhancement near the slot [49]. In order to eliminate any field enhancement near the slot, another coupling scheme was adopted to separate the rf coupler from the DLA structure [43,50–51]. There are three sections in this scheme: an rf coupler section, a tapered dielectric matching section, and a uniform DLA section. Both dielectric matching section and DLA section were fabricated separately and then assembled mechanically. But breakdown occurred at the dielectric joints between separate dielectric sections. A microscale vacuum gap in the dielectric joint may result in the breakdown due to a strong local field enhancement in it. In order to eliminate dielectric joints, a new type of structure was developed using a clamped copper outer jacket to enclose a whole dielectric tube including a matching section and a DLA section. Such a structure has been used for many high-power experimental studies [41–43,45–46]. In [41,45] a strong multipactor was observed in a tapered dielectric matching section with a length of >30 mm. At this length, it is a big challenge to completely suppress the multipactor, requiring a large solenoidal magnet capable of producing a uniform axial magnetic field over the whole DLA structure with a tapered dielectric matching section. This length also occupies valuable space which could be saved for accelerating structures. Thus, a compact matching section with a much shorter length would, if realized, represent an advance for externally powered DLA structures.

Since the late 1980s researchers from SLAC and KEK have been pioneering the development of accelerating structures at *X*-band (11.424 GHz, 4 times the frequency of the SLAC Linac) for a TeV-scale e^+e^- linear collider in the framework of Next Linear Collider (NLC) and Global Linear Collider (GLC) project [52–56]. An accelerating gradient of 65 MV/m with 400 ns long pulses was achieved [57–59] at the end of the NLC/GLC program. In 2004, a key decision was made by the International Technology Review Panel (ITRP) to select L-band (1.3 GHz) superconducting technology for the International Linear Collider (ILC) [60]. There was a slow-down for the development of *X*-band technology afterwards. However, in 2007 CERN decided to lower the frequency of the Compact Linear Collider (CLIC) to 12 GHz (previously at 30 GHz) [61], resulting in a renewed and vigorous interest in *X*-band technology. To date, the undamped design of CLIC *X*-band traveling-wave structures named T24 has obtained a gradient of 120 MV/m with a pulse length of 200 ns [5,62–63]. This gradient is far beyond those reached with the present S-band and C-band technology. Today *X*-band technology is rapidly expanding in the communities of linear collider [64–71], light-source [72–76], medical therapy [77–79].

Building on these developments, a DLA structure operating at *X*-band appears to be very promising for future linear accelerators. We describe in this paper a detailed design, fabrication, and low-power rf measurement of an *X*-band DLA structure with a compact dielectric matching section. In order to efficiently couple the rf power from a rectangular waveguide to an *X*-band DLA structure, three modules are adopted (see Fig. 1): a main DLA module at center sandwiched by two mode converter modules towards rectangular waveguide. The mode converter module consists of two sections, a symmetrical feeding dual ports converting the rectangular TE_{10} mode to the circular TM_{01} mode, and a choke connection toward the DLA module side. The DLA module consists of three sections, the main, uniform DLA section connected to the compact dielectric matching sections at both ends being extended by circular pipe to the connection to the converter module. The compact dielectric matching section provides a good match for the impedance of the TM_{01} mode between the circular waveguide and the DLA structure. A choke flange separates the DLA structure from the mode converter and thus
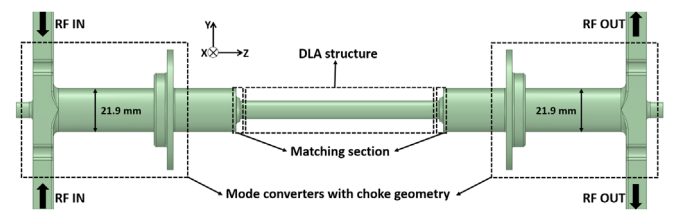

FIG. 1.   Conceptual illustration of an externally powered DLA structure connected with two matching sections and two TE_{10}-TM_{01} mode converters with choke geometry.

makes the mode converter independent of the dielectric properties. In this case, the mode converter can be reused for similar experiments operating at the same frequency. Section II presents detailed rf design of an *X*-band DLA structure and compact dielectric matching sections using MgTiO$_3$ ceramic. Section III shows the fabrication process for obtaining the prototypes of mode converters and DLA structure. Section IV presents the low-power rf measurement for the full-assembly prototypes and its comparison with the simulations. Section V investigates the fabrication errors to cause the discrepancy between measurements and the simulations. Section VI gives the conclusions.

II. DESIGN OF AN *X*-BAND DLA STRUCTURE AND DIELECTRIC MATCHING SECTIONS

In this section, the rf properties of an *X*-band DLA structure (see Fig. 2) are studied. A compact dielectric matching section to efficiently couple the rf power from a circular waveguide into the DLA structure is also described in detail.

A. A DLA structure

MgTiO$_3$ ceramic, with good thermal conductivity and ultralow power loss, which has been studied in [28], is chosen as the dielectric material for our DLA structure. An accurate measurement of the dielectric properties has to be performed before using such a ceramic for our rf design. As shown in Fig. 3, a TE$_{01\delta}$ silver-plated resonator [80], which is designed for testing ceramics at an *X*-band frequency, is used to measure the dielectric constant ε_r and loss tangent $\tan\delta$ of sample coupons. Four coupons made from the same dielectric rods as for the fabrication are measured. A dielectric constant $\varepsilon_r = 16.66$ and a loss tangent $\tan\delta = 3.43 \times 10^{-5}$ (having error bars 0.6% of the nominal value) are obtained for the rf design of the DLA structure and matching sections which follow.

The DLA structure could be potentially used for the CLIC main linac [64–69]. The inner radius is chosen to be $R_{in} = 3.0$ mm from consideration of the CLIC beam
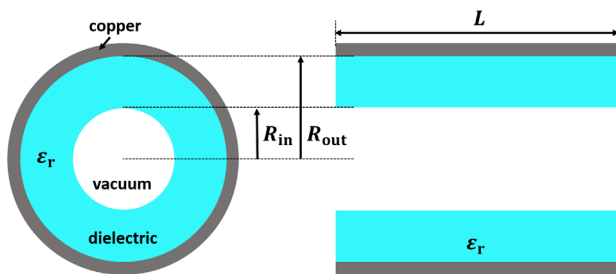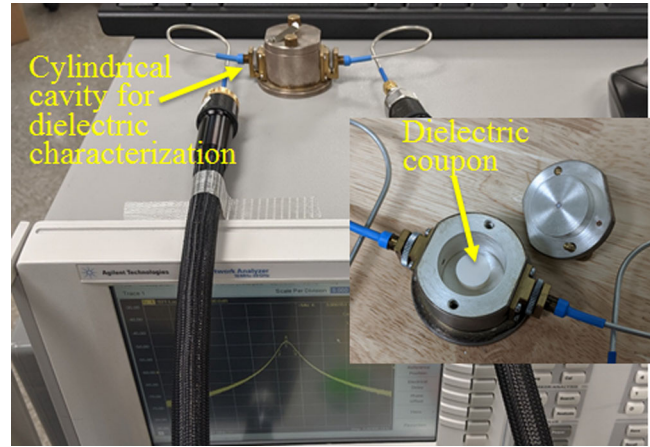

FIG. 3. Measurement setup of the dielectric properties of the material sample.

dynamics requirement [66,67]. The outer radius is then calculated to be $R_{out} = 4.6388$ mm for an operating frequency of $f_0 = 11.994$ GHz. The group velocity obtained is $v_g = 0.066c$, where *c* is speed of light. A quality factor of $Q_0 = 2829$ and a shunt impedance of $R_{shunt} = 26.5$ MΩ/m are also derived for such a DLA structure using HFSS [81]. The length of the DLA structure is chosen as $L = 100$ mm for the following simulations and mechanical assembly.

B. A compact dielectric matching section

A clamped copper outer jacket enclosing a tapered matching section and a DLA section [43] has been successfully used for many high-power experimental studies [41–43,45–46]. But this matching section has a length of >30 mm as compared to the DLA length of ~100 mm [41,45]. Therefore, a compact matching section would be very advantageous given that it saves the valuable space for the DLA section.

Through optimization studies [82], a compact dielectric matching section is obtained: $W_1 = 2.035$ mm, $H_2 = 2.74$ mm, $\theta = 60°$, $R_f = 2.0$ mm, and $R_m = 0.5$ mm, as shown in Fig. 4. In fabrication, a sharp dielectric corner easily breaks. In order to prevent such a break, a 45° chamfer with a length of 0.254 mm is added to this corner, as shown in Fig. 4. The shape of the outer metal is also changed by rounding with a fillet radius of $R_r = 0.322$ mm, in order to prevent field enhancement near that area.

Figure 5(a) shows the simulated electric field distribution for the compact dielectric matching section at an input power of 1 W. Figure 5(b) indicates that the electric fields near that area are much lower than those of the DLA structure. In this case, this dielectric matching section has the potential to survive at a similar high-power level >5 MW [42–43,45–46].

Figure 6 shows the simulated $S_{11} = -48$ dB and $S_{21} = -0.31$ dB for the compact dielectric matching section at the operating frequency of 11.994 GHz. Using $S_{21} = -0.31$ dB,

FIG. 2. Front view and longitudinal cross section of a cylindrical DLA structure. ε_r, R_{in}, R_{out}, and *L* represent dielectric constant, inner radius, outer radius, and length for the DLA structure.
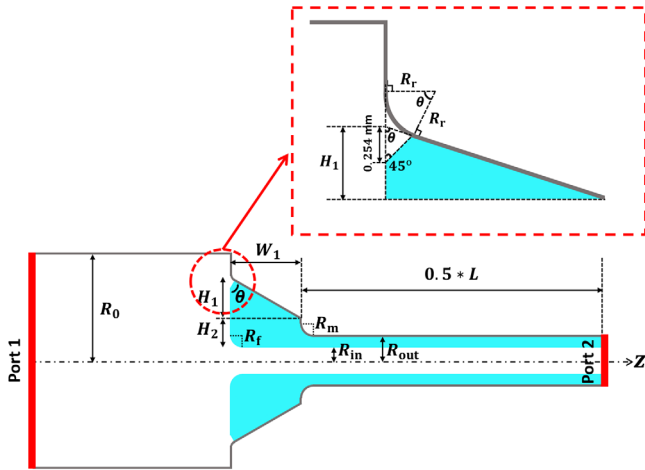
FIG. 4.   Longitudinal cross section of a circular waveguide, a compact dielectric matching section, and a DLA structure.
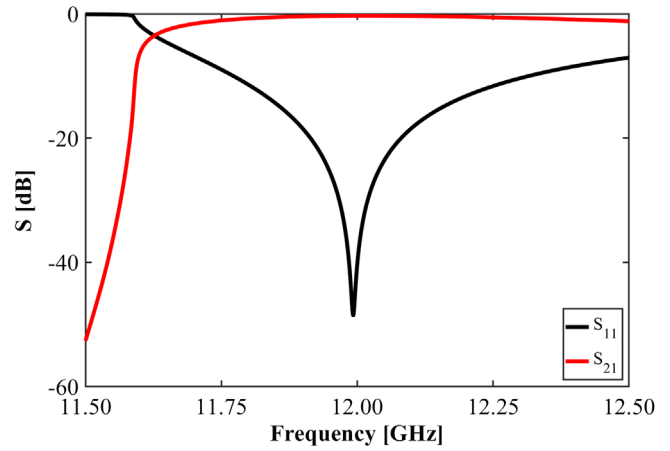

FIG. 6.   Simulated S_{11} and S_{21} as a function of frequency for the compact dielectric matching section.
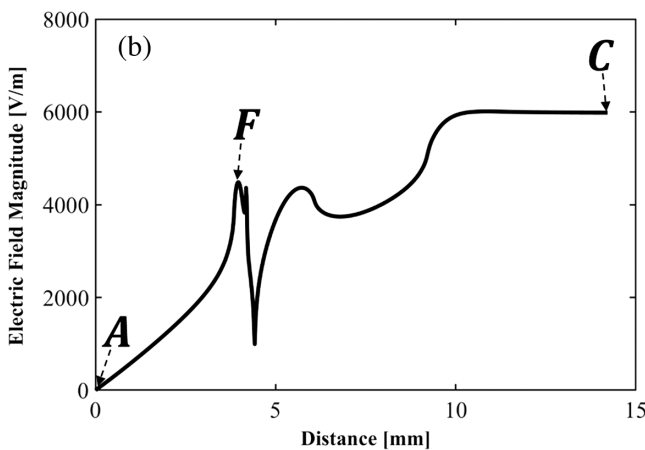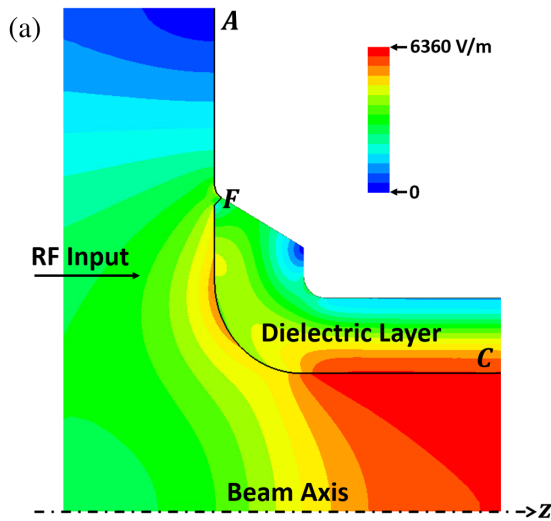

FIG. 5.   (a) Electric field distribution for the compact dielectric matching section with a chamfered corner. (b) Electric field magnitude along path AFC which denotes a section of lines and arcs connected by the points A, F, and C, as shown in (a), where the distance of point A is taken as 0 mm.

the coupling coefficient (it is defined by $\eta = 10^{\frac{S_{21}}{5}}$ and frequently used in the analysis in this paper) for the whole dielectric structure is calculated to be 86.7%. The S_{21} also has a broad 3 dB bandwidth of more than 1.0 GHz, which allows greater tolerance to potential fabrication errors.

C. A design gap

In our fabrication, the entire dielectric tube, including the matching section and the DLA structure, is machined as a single piece. A thin metallic layer of 0.0508 mm is first coated onto the surface of the whole dielectric tube in order to keep in close touch with the outer copper jacket. The coated dielectric tube is then inserted into the outer copper jacket. However, a microscale gap is needed in the tapered area between the thin metallic coating and the outer thick copper jacket for proper clamping, as shown in Fig. 7. It is therefore of particular importance to study the dependence of the S parameters and electric fields on the design gap d_2.

Figure 8 shows how varying the design gap d_2 influences S_{11} and S_{21}. With a larger design gap, S_{11} increases while S_{21} remains almost unchanged, resulting in worse matching. For a design gap of $d_2 = 0.2$ mm, $S_{11} = -31.5$ dB and $S_{21} = -0.31$ dB are obtained. S_{11} is increased to -28 dB and S_{21} stays almost constant, when the design gap becomes 0.3 mm.

Figure 9(a) shows the simulated electric field distribution for the matching section with a design gap, at an input power of 1.0 W. Figure 9(b) gives the simulated electric field magnitude along path AGC for different design gaps. There are two peaks in each curve, indicating the relatively strong fields near the chamfered corner and rounding corner, respectively. For a design gap of 0.3 mm, the peak fields are higher than those of the DLA structure, which may cause arcing in a high-power test. The dielectric matching section is therefore allowed to have a maximum design gap of 0.2 mm, in which rf fields are still lower than
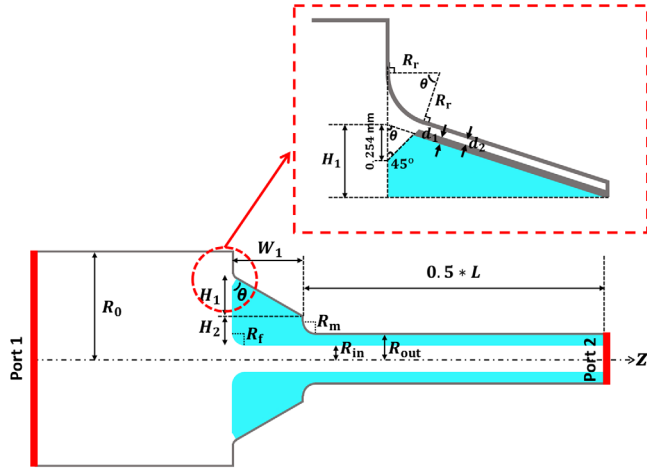
FIG. 7. Longitudinal cross section of a circular waveguide, a compact dielectric matching section with a design gap, and a DLA structure.
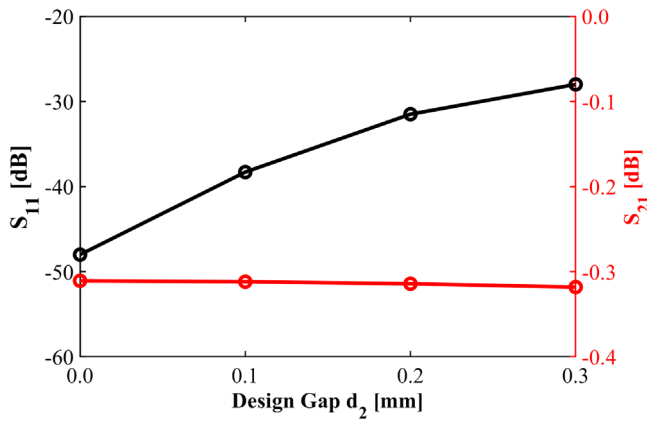

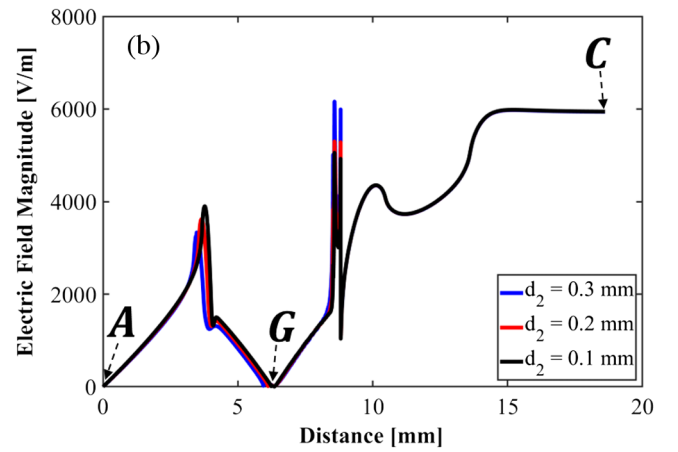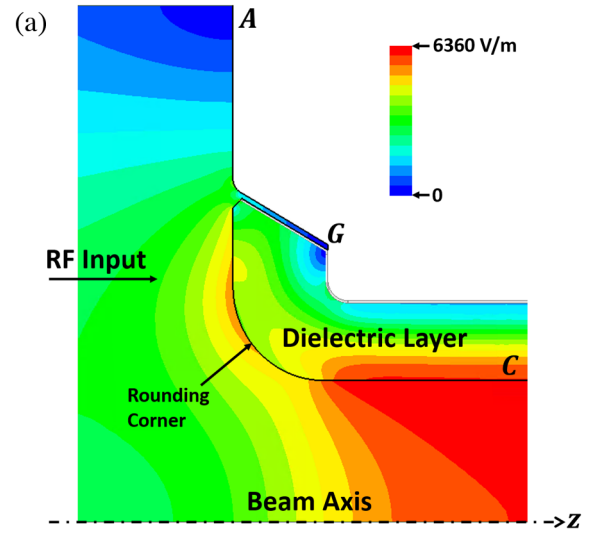FIG. 8. Simulated S_{11} and S_{21} as a function of design gap d_2.

FIG. 9. (a) Electric field distribution for the dielectric matching section with a design gap, where the thin metallic coating is denoted by the white lines. (b) Electric fields magnitude along path AGC for different design gaps d_2. Here path AGC denotes a section of lines and arcs connected by the points A, G, and C, as shown in (a), where the distance of point A is taken as 0 mm.

those of DLA structure. This value is used to accept the fabrication tolerances of the copper jacket and the metallic coating of the dielectric tube.

D. Tolerance studies

Through optimization studies [82], geometrical parameters for the dielectric matching section and the DLA structure are obtained as follows: $\varepsilon_r = 16.66$, $W_1 = 2.035$ mm, $H_2 = 2.74$ mm, $\theta = 60°$, $R_f = 2.0$ mm, $R_m = 0.5$ mm, $R_{out} = 4.6388$ mm, $R_{in} = 3.0$ mm, and $L = 100$ mm. Using these geometrical parameters, $S_{11} = -48$ dB and $S_{21} = -0.31$ dB are achieved at an operating frequency of 11.994 GHz. It should be noted here that both S parameters include the copper circular waveguide and the DLA structure with a dielectric matching section (see Figs. 4 and 7).

As we know, S_{21} for the matching section has a large 3 dB bandwidth of over 1 GHz, so it is not sensitive to changes in the geometrical parameters. The tolerances are studied by calculating the dependence of S_{11} on the geometrical parameters. By adjusting a certain geometrical parameter from x to $x \pm dx$, S_{11} is simulated and compared with the setting requirements of -30, -25, and -20 dB. The length of the DLA structure does not have any effect on the S parameters and rf-field performance, so it is ruled out for tolerance studies in this section. The tolerances of key geometrical parameters (see Table I) are discussed in detail.

As shown in Table I, S_{11} is very sensitive to W_1, R_{out}, and R_{in} and less sensitive to ε_r, H_2, θ, R_f, and R_m. The dielectric fabrication accuracy should be better than ±0.02 mm in order to realize a $S_{11} \leq -20$ dB. This is very challenging but it is still feasible from the previous fabrication experience [83]. The acceptance criteria for coupling coefficient is assumed to be $\eta \geq 80\%$ in this paper. In the worst case, S_{21} is found to be $S_{21} \geq -0.45$ dB, enabling the coupling

TABLE I. The tolerances of geometrical parameters for the dielectric matching section and DLA structure.

$f_0 = 11.994$ GHz	$S_{11} \leq -30$ dB	$S_{11} \leq -25$ dB	$S_{11} \leq -20$ dB
$\varepsilon_r = 16.66$	$[-0.079, +0.081]$	$[-0.139, +0.148]$	$[-0.24, +0.27]$
$W_1 = 2.035$ [mm]	$[-0.007, +0.007]$	$[-0.012, +0.012]$	$[-0.022, +0.022]$
$H_2 = 2.74$ [mm]	$[-0.015, +0.017]$	$[-0.027, +0.030]$	$[-0.051, +0.054]$
$\theta = 60^\circ$	$[-2.5^\circ, +2.0^\circ]$	$[-4.3^\circ, +3.7^\circ]$	$[-7.3^\circ, +7.0^\circ]$
$R_f = 2.0$ [mm]	$[-0.042, +0.040]$	$[-0.076, +0.068]$	$[-0.140, +0.120]$
$R_m = 0.5$ [mm]	$[-0.061, +0.049]$	$[-0.118, +0.090]$	$[-0.245, +0.151]$
$R_{out} = 4.6388$ [mm]	$[-0.0076, +0.0065]$	$[-0.0123, +0.0127]$	$[-0.020, +0.025]$
$R_{in} = 3.0$ [mm]	$[-0.006, +0.007]$	$[-0.012, +0.012]$	$[-0.024, +0.020]$

coefficient of 81.3%. This is still acceptable for efficient coupling for high-power experiment on DLA structures.

E. A full-assembly structure

In this section, a full-assembly structure (see Fig. 10) is obtained by adding the DLA structure connected together with two matching sections, circular waveguides with the choke geometry, and the TE_{10}-TM_{01} mode converters. The mode converters and choke geometry have been studied in [82,84]. The rf performance of such a full-assembly structure is described in detail. The whole structure is simulated by analyzing the electric field distribution and S parameters from port $1'$ to port $2'$. rf power loss on both the metallic surface and in dielectrics and accelerating fields in the vacuum channel are also studied in detail.

Figure 11 gives simulated values of $S'_{11} = -40$ dB and $S'_{21} = -0.67$ dB for the full-assembly structure at the operating frequency of 11.994 GHz. It should be noted here that S'_{11} and S'_{21} denote the reflection coefficient and transmission coefficient, respectively, between ports $1'$ and $2'$, as shown in Fig. 10. S'_{ij} $(i, j = 1, 2)$ with apostrophe [see Figs. 10,16(b),18(b),21,23, and 25] is different from S_{ij} without apostrophe which indicates S parameters between ports 1 and 2 [see Figs. 16(a) and 18(a)]. Using the power density on the metallic surface and in the dielectric area for an input power of 1.0 W, the calculated rf power loss on the metallic surface is $P_{loss\_surface} = 0.130$ W and the rf power loss obtained in dielectrics is $P_{loss\_dielectric} = 0.012$ W. So the total rf power loss is $P_{total\_loss} = 0.142$ W. The output rf power at port 2 is $P_{out} = 0.858$ W. We thus achieve a transmission coefficient $S'_{21} = 10 \log(P_{out}/P_{in}) = -0.67$ dB, which agrees well with the simulated S'_{21} shown in Fig. 11. At the maximum peak power of 40 MW from XBOX [85–86] with a pulse width of 1.5 μs and a repetition rate of 50 Hz an average input power of 3.0 kW will be generated. The power loss on the metallic surface is then 390 W and the power loss in dielectrics is 36 W. A water cooling system is thus required for the high-power test on the full-assembly structure.

Figure 12 shows the electric field magnitude along a line MN (see Fig. 10). The electric fields are gradually becoming weaker, due to rf power loss in the dielectric and on metallic surfaces, as the rf fields propagate from point M to point N. The average accelerating gradient is calculated to be 5773 V/m at an input power of 1.0 W. For a power of 40 MW from XBOX, an average accelerating gradient of 36.5 MV/m can be achieved for our DLA structure.

Figure 13 presents the full-assembly mechanical design for the whole structure. The gray area denotes the outer copper jacket, connected with openings to avoid air
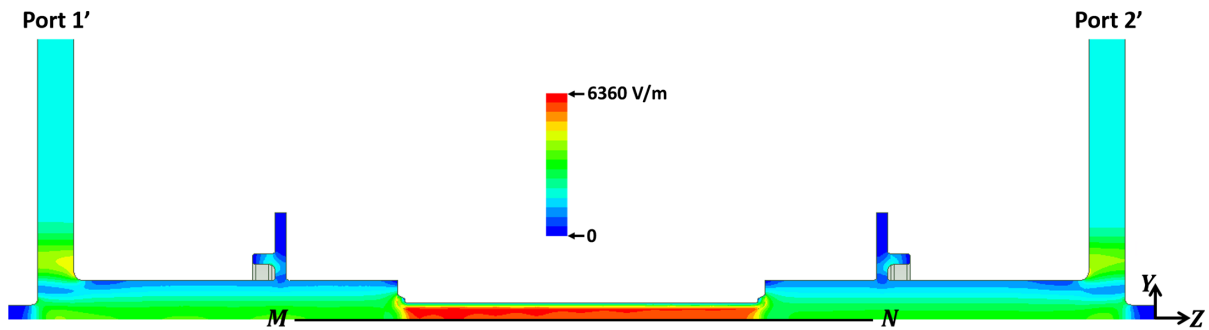

FIG. 10. Electric field distribution for the full-assembly structure with a quarter geometry, where line MN is located on the center along the z axis.
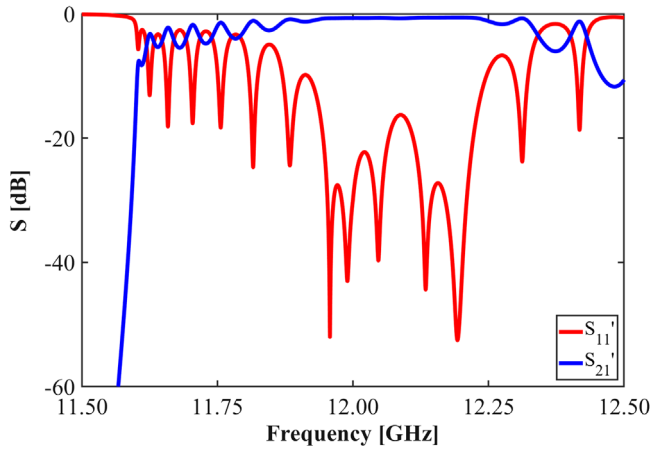
FIG. 11. Simulated S'_{11} and S'_{21} as a function of frequency for the full-assembly structure shown in Fig. 10.
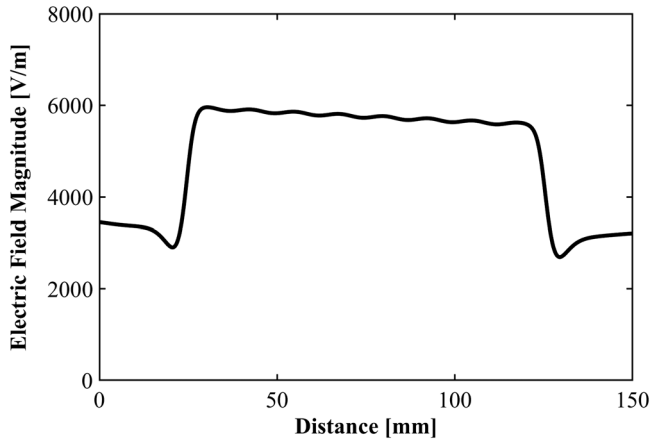

FIG. 12. Electric field magnitude along the line MN shown in Fig. 10. The distance of point M is taken as 0 mm.

trapping when pumping. Two conflat flanges are used to connect the center part with the end parts, which are TE_{10}–TM_{01} mode converters with half-choke geometry.

III. FABRICATION

A. TE_{10}–TM_{01} mode converter with half-choke geometry (end-part prototype)

The TE_{10}–TM_{01} mode converter with half-choke geometry (also called as end-part prototype, see Fig. 13) was fabricated by the CERN workshop using conventional welding and brazing. The fabricated end-part prototypes are shown in Fig. 14. Two mode converters with half-choke [see Fig. 14(a)] which have exactly the same geometry are used for the full-assembly structure. Figure 14(b) shows the copper half-choke geometry and the stainless-steel conflat flange. The screws are used to tighten both flanges between the center-part prototype and two end-part prototypes.

B. Dielectric structure facing half-choke geometry (center-part prototype)

The fabrication started from a sintered single piece ceramic rod and witness samples for the characterization measurement. Then the rod was machined to a dielectric tube with required dimensions in a professional ceramic machining company Insaco [83]. The whole dielectric tube has a thin coating silver layer of 0.0508 mm on its outer surface including the matching section and DLA structure. It should be noted here that the inner surface and other area do not have any coating. This coating is specially used for maintain good contact with the outer copper jacket. The coated dielectric tube is then inserted into the outer copper jacket which consists of two-halves parts, as shown in Fig. 15(a). These two-halves parts are connected in the absence of brazing, forming a microgap, as shown in Fig. 15(b). Such a microgap may break the rotational symmetry of the whole structure. The ideal case is that there is no offset for the two-halves copper jacket in both
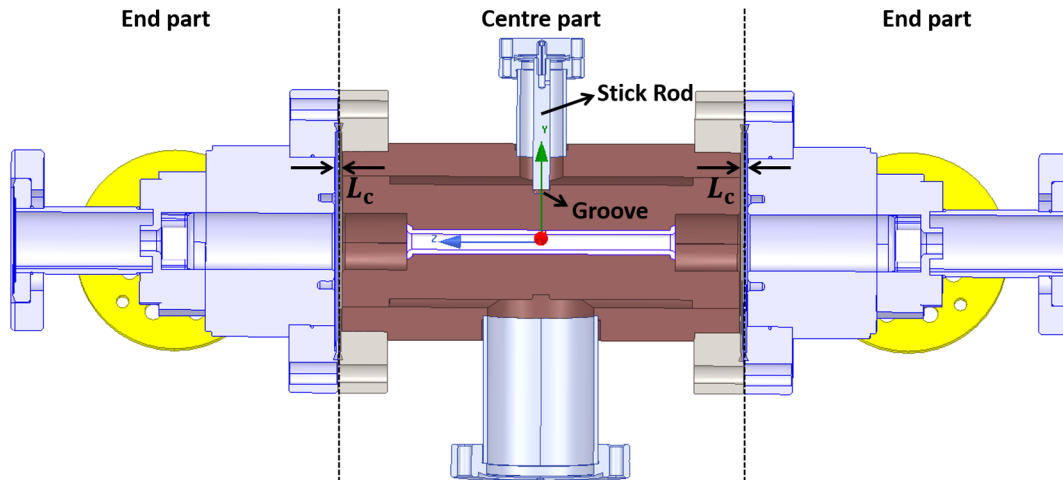

FIG. 13. Full-assembly mechanical design for the whole structure, including a center part and two end parts.
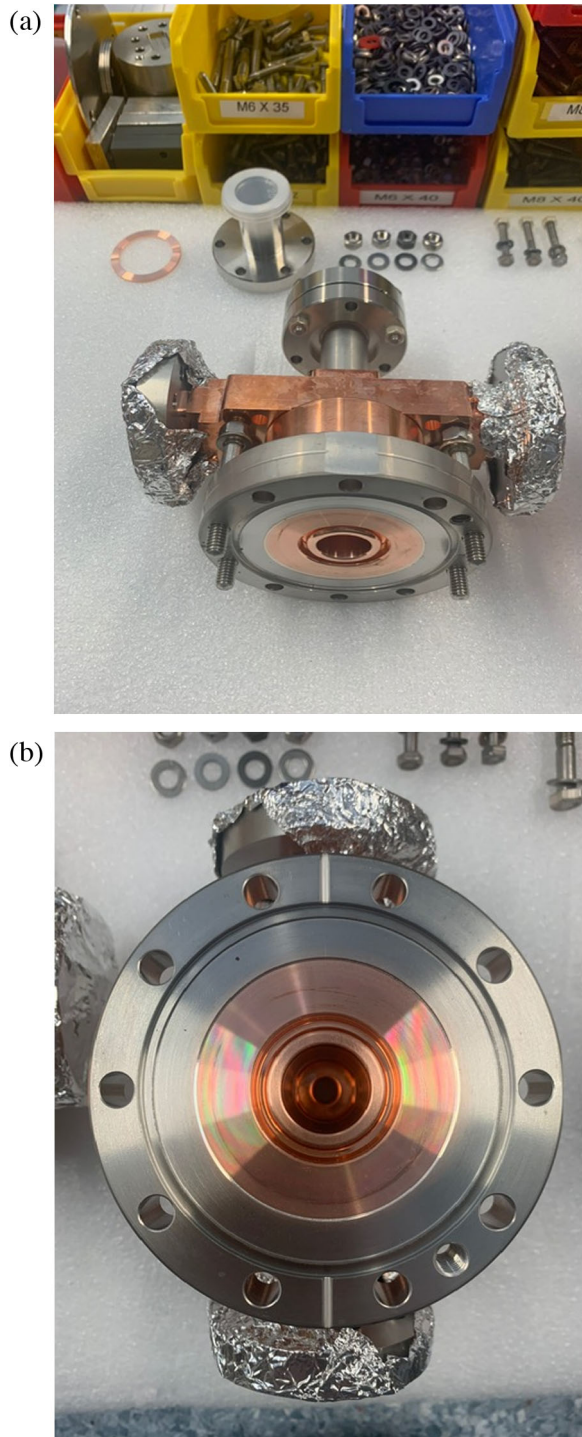
FIG. 14. Prototypes of the mode converter with half-choke geometry (a) and conflat flange (b).

FIG. 15. (a) The coated dielectric tube is put into the outer copper jacket. (b) The assembly center-part prototype with the vacuum housing.

horizontal (x-axis) and vertical (y-axis) directions. For a microgap of 0.15 mm and the worst symmetry braking (an alignment angle $\beta = 45°$), the simulated $S'_{11} = -35$ dB, $S'_{21} = -0.75$ dB. S'_{21} can be decreased to -1.8 dB when this microgap equals to 1.0 mm. It should be noted here that the reflection coefficient $S'_{11} = (S_{11} + S_{13} + S_{31} + S_{33})/2$
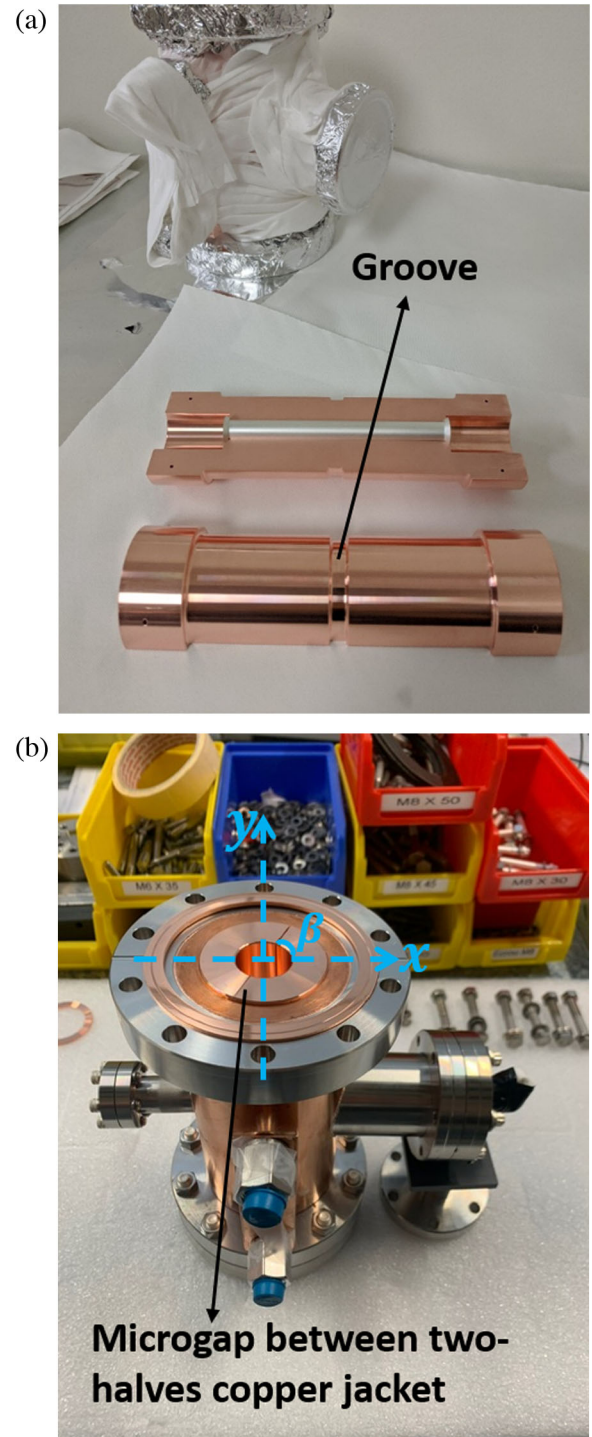
and transmission coefficient $S'_{21} = (S_{21} + S_{23} + S_{41} + S_{43})/2$ for a full-assembly structure with four ports (ports 1, 2, 3, and 4), where S_{ij} ($i, j = 1, 2, 3, 4$) are S parameters for this four-port structure. However, this asymmetry can be mitigated by introducing symmetrical power splitters into

TABLE II. Different kinds of assembly for measurement.

Different kinds of assembly	VNA	Subsection
Two end-part prototypes + aluminum waveguide	Four-port VNA	Subsection A
Two end-part prototypes + center − part prototype (DLA structure)	Four-port VNA	Subsection B
Two end-part prototypes + aluminum waveguide + power splitters	Two-port VNA	Subsection C
Two end-part prototypes + center − part prototype (DLA structure) + power splitters	Two-port VNA	Subsection C and subsection D

the whole structure. The vacuum housing is clamped with the outer copper jacket, forming the center-part prototype, as shown in Fig. 15(b). This center-part prototype has two conflat flanges at both sides which can be tightened together with mode converters to form an ultrahigh vacuum.

It should be noted that the outer copper jacket easily slides along the longitudinal direction inside the vacuum housing. In this case, the choke gap L_c (see Fig. 13) at both sides is changed accordingly, which will be discussed in Sec. IV D. Therefore, a stainless-steel stick rod (see Fig. 13) is inserted into the groove [see Fig. 15(a)] of the outer copper jacket in order to stop it from moving along the longitudinal direction. This stick rod is integrated with the flange inside the vacuum housing.

IV. LOW-POWER RF MEASUREMENT

In this section, we describe the process and the results of low-power rf measurement performed for the full-assembly structure by using a vector network analyzer (VNA). As shown in Table II, three different kinds of assembly were measured by either a four-port or a two-port VNA. This section follows the order of each row in this table for the measurements.

A. Assembly of two end-part prototypes and an aluminum waveguide

In order to verify the measurement, an aluminum waveguide is fabricated with the same inner radius of the cylindrical waveguide. The outer radius of this waveguide is the same as that of the conflat flange. Such an aluminum waveguide is assembled with two end-part prototypes, as shown in Fig. 16(a). A four-port VNA is used to measure this assembly structure. It should be noted here that the aluminum waveguide is replacing the DLA part in the measurement. Given the symmetry of the assembly structure, a quarter of the structure is modeled and simulated in HFSS, as shown in Fig. 16(b).

The four-port S parameters can be transformed into the two-port S parameters when the network has a quarter symmetry. Figure 17 shows that the measured $S'_{11} = -34.4$ dB and $S'_{21} = -0.26$ dB while the simulated $S'_{11} = -57.9$ dB and $S'_{21} = -0.05$ dB at the operating frequency of 11.994 GHz. It is found that the measurements are different from the simulations, which may be caused by

fabrication errors. However, the measured S parameters are still acceptable in terms of rf power transmission (coupling coefficient is 94.2% > 80%) from ports 1' and 2'. Therefore, it is concluded that most of the rf power propagates through the end-part prototypes in a normal way.

B. Assembly of two end-part prototypes and center-part prototype

After confirming the end-part prototypes work well, we move on to assemble two end-part prototypes and center-part prototype together, as shown in Fig. 18(a). Figure 18(b) shows the modeling of the full-assembly geometry in HFSS
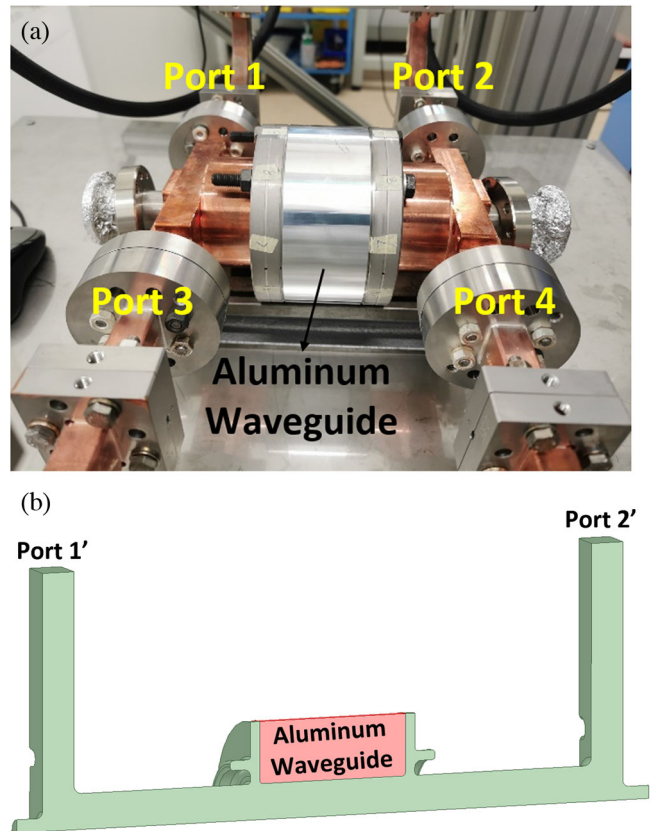

FIG. 16. The mechanical assembly (a) and simulation modeling (b) of two end-part prototypes and an aluminum waveguide (see first row of Table II).
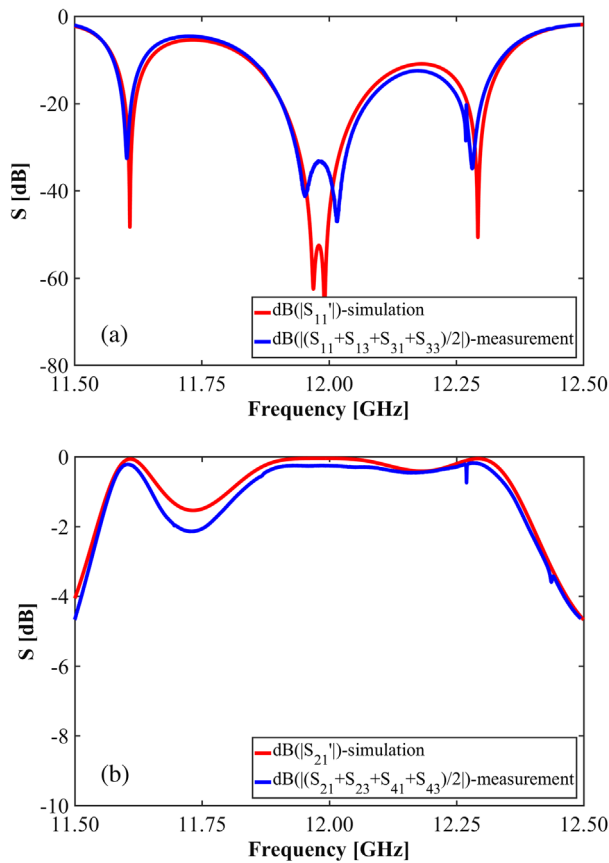
FIG. 17. Comparison between simulated and measured S-parameters [(a) S'_{11} and (b) S'_{21}] for two end-part prototypes connected with an aluminum waveguide.
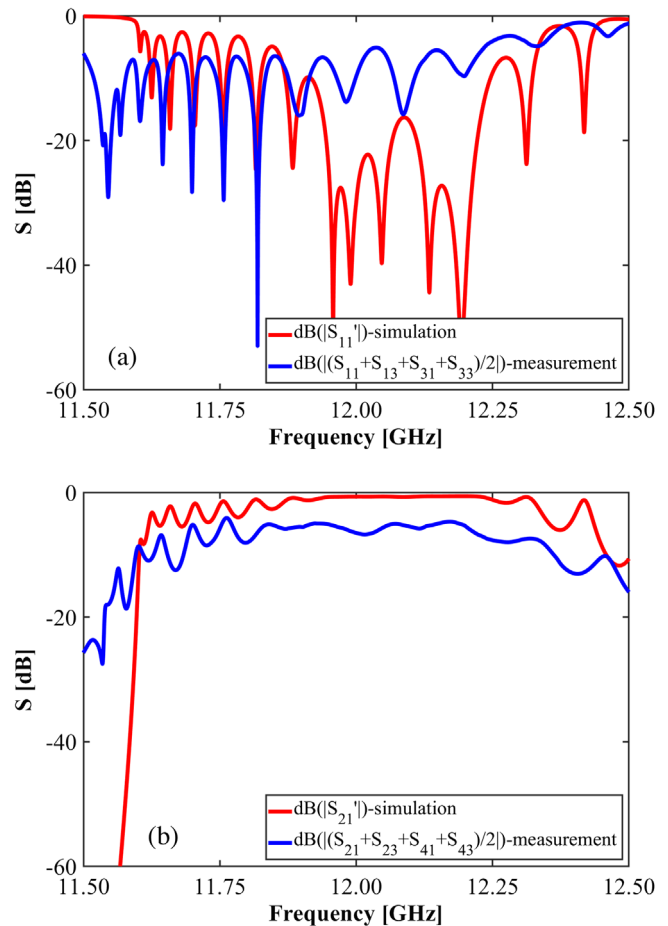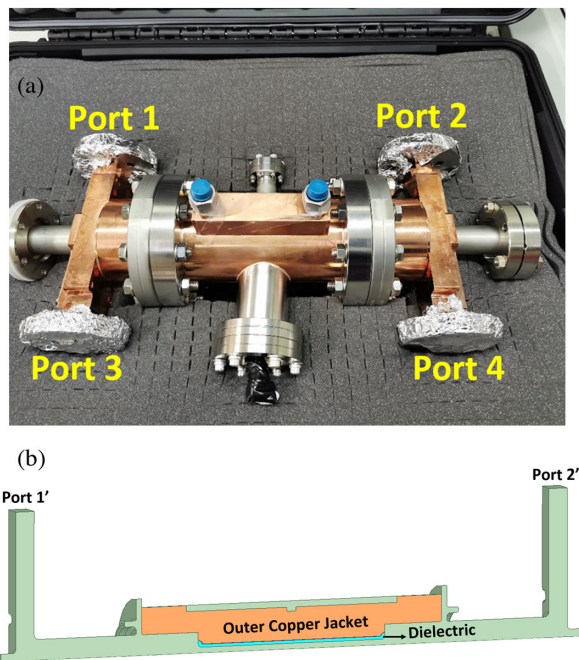

FIG. 18. The mechanical assembly (a) and simulation modeling (b) of two end-part prototypes and center-part prototype (see second row of Table II).

FIG. 19. Comparison between simulated and measured S-parameters [(a) S'_{11} and (b) S'_{21}] for the full-assembly structure.

simulations, which will be used for comparing with measurements.

Figure 19 shows that measured $S'_{11} = -11.3$ dB and $S'_{21} = -6.3$ dB while simulated $S'_{11} = -40$ dB and $S'_{21} = -0.67$ dB at the operating frequency of 11.994 GHz. It is obvious that there is a significant discrepancy between measurements and simulations. This discrepancy may be caused by fabrication errors for the DLA structure with the matching sections and microgap between the two-halves copper jacket. Investigations into possible reasons for the discrepancy will be discussed in Sec. V.

In order to know the electric field distributions along the axis in the full-assembly structure, the bead-pull measurement is carried out as follows. In the measurement, a small dielectric bead attached to a string is pulled on axis through the whole structure while a low rf power is fed into the structure at the frequency of 11.994 GHz. Dry nitrogen is fed into the structure to avoid permittivity errors due to humidity changes. An electric field profile can be obtained by calculating the change of reflection coefficient with respect to the bead position.

Based on [87–88], the square of electric field strength E^2 is proportional to the change of reflection coefficient
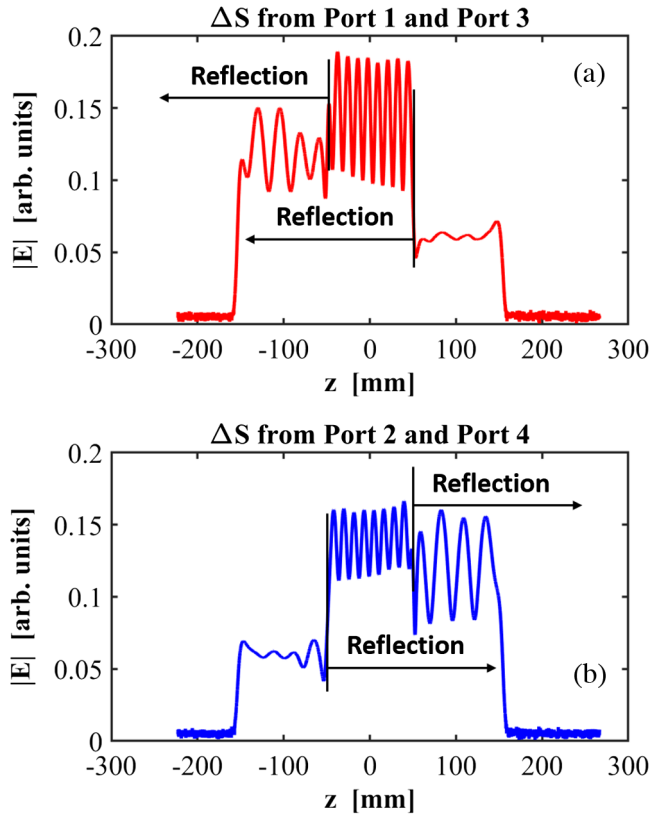
FIG. 20. Measured electric field magnitude for injecting rf power from ports 1 and 3 (a), and from ports 2 and 4 (b), respectively.

FIG. 21. The assembly of two end-part prototypes and an aluminum waveguide connected with two power splitters (see third row of Table II).

$\Delta S = S - S^0$, where S is the reflection coefficient and S^0 is the zero-line fitting function. Our full-assembly structure is a four-port network. The reflection coefficient $S = (S_{11} + S_{13} + S_{31} + S_{33})/2$ for ports 1 and 3 while $S = (S_{22} + S_{24} + S_{42} + S_{44})/2$ for ports 2 and 4, where S_{11}, S_{13}, S_{31}, S_{33}, S_{22}, S_{24}, S_{42}, S_{44} are scattering parameters for our four-port network. Figure 20 shows the measured electric field distribution on the beam axis of structure at the operating frequency of 11.994 GHz. The red curve denotes the electric field distribution for the case of injecting rf power from ports 1 and 3 while the blue curve denotes the electric field distribution for the case of injecting rf power from ports 2 and 4. The difference between them demonstrates that the whole structure is asymmetrical because of fabrication error and microgap between the two-halves copper jacket. It can also be clearly seen that there are reflections at the position of matching sections for both cases. These reflections may also be caused by fabrication errors for the matching sections, which will be discussed in Sec. V.

C. Add power splitters for the assembly of two end-part prototypes and center-part prototype

In previous subsections, we know the fabrication errors and microgap between the two-halves copper jacket may break the symmetry of the whole structure. In this case,
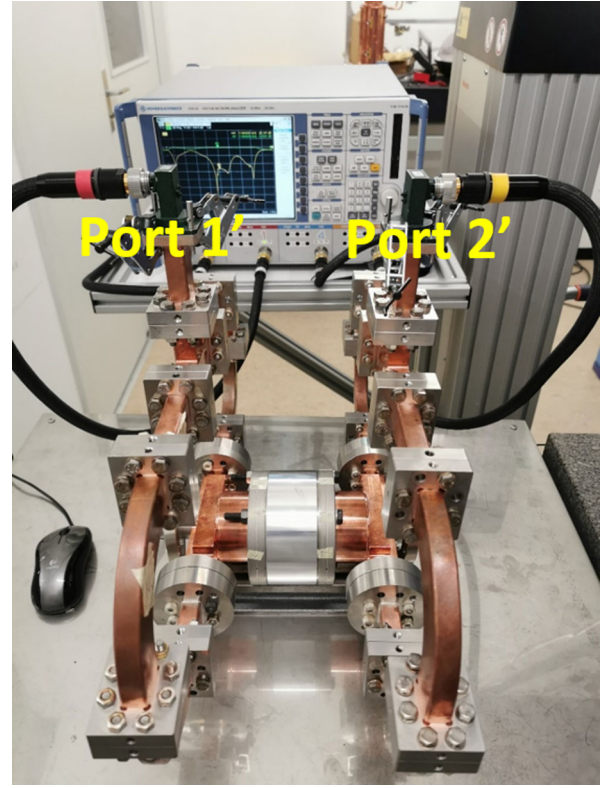
dipole TE_{11}-type modes are excited and propagate through the DLA structure in our previous measurements. This may result in a high-power loss. In order to prevent the potential dipole modes and remove the influence of microgap, two power splitters are added into the rf measurement.

At first, two power splitters are added for the assembly of two end-part prototypes and an aluminum waveguide. The four-port network is changed to a two-port network. The low-power rf measurement is carried out for this two-port network, as shown in Fig. 21.

Figure 22 shows measured $S'_{11} = S'_{22} = -26.1$ dB and $S'_{12} = S'_{21} = -0.2$ dB at the operating frequency of 11.994 GHz. It can be clearly seen that both S'_{11} and S'_{12} agree well with S'_{22} and S'_{21}. This indicates that the power splitters are symmetrical for rf propagating, thereby resulting in a small reflection coefficient and negligible transmission loss. In this measurement, dipole modes are fully suppressed in the structure.

After confirming that power splitters work smoothly, we replace the aluminum waveguide with the center-part prototype which has a DLA structure inside. As shown in Fig. 23, similar rf measurement is carried out for this full-assembly structure.

Figure 24 shows measured $S'_{11} = -15.2$ dB, $S'_{22} = -10.2$ dB, $S'_{12} = S'_{21} = -4.96$ dB at the operating frequency of 11.994 GHz. S'_{11} does not agree well with
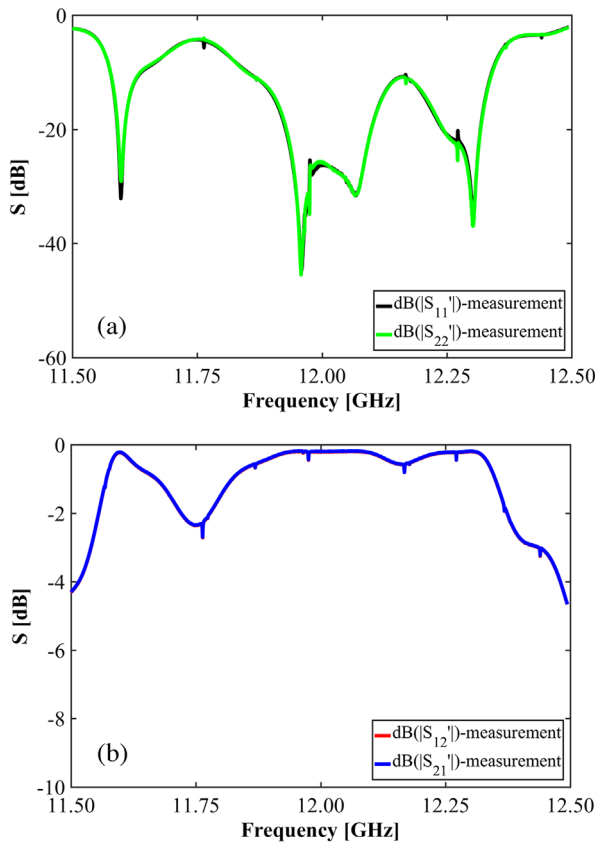
FIG. 22. Comparisons between measured (a) S'_{11} and S'_{22}, (b) S'_{12} and S'_{21} for two end-part prototypes connected with an aluminum waveguide and two power splitters.
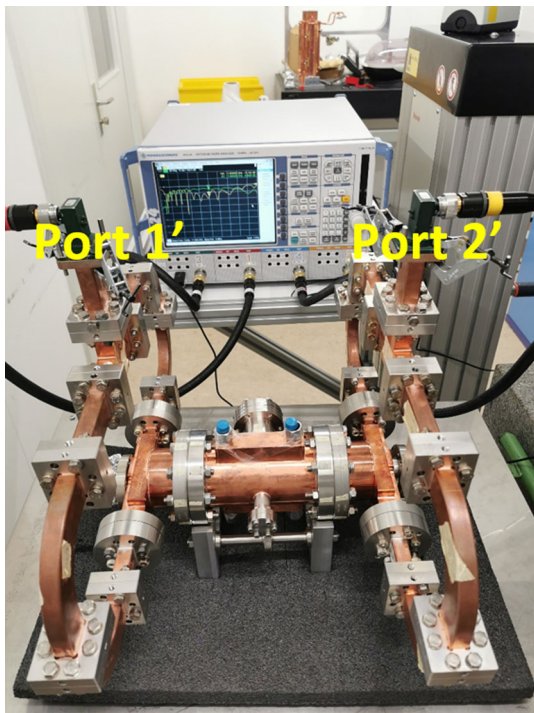

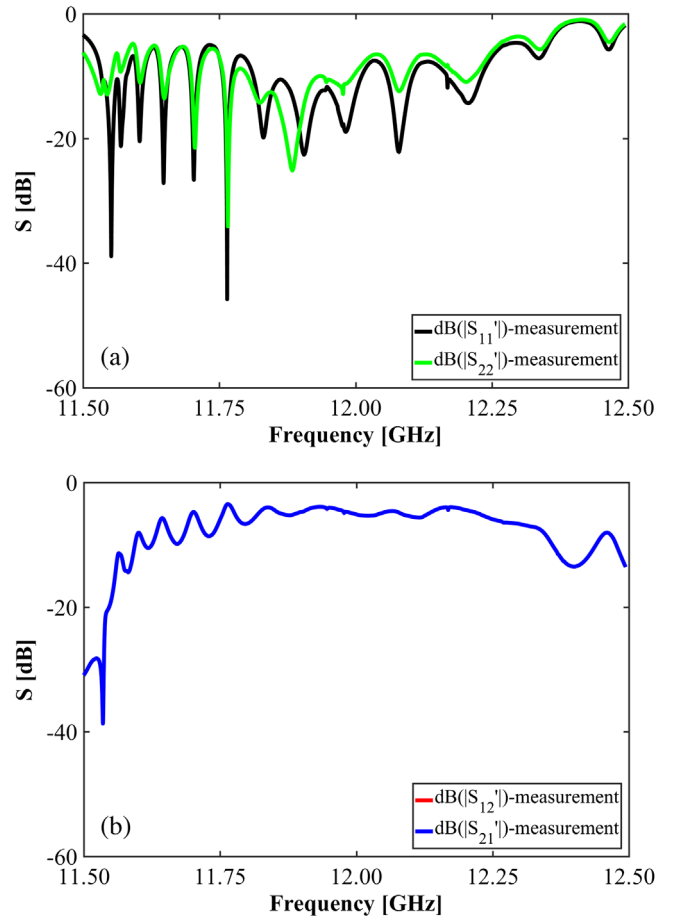FIG. 23. The full-assembly structure connected with two power splitters (see fourth row of Table II).

FIG. 24. Comparisons between measured (a) S'_{11} and S'_{22}, (b) S'_{12} and S'_{21} for the full-assembly structure with two power splitters.

S'_{22}, which is probably due to asymmetry of the full-assembly structure. Both S'_{11} and S'_{21} are improved as compared to previous four-port measurements (see Fig. 19). This indicates that symmetrical power splitters are beneficial for suppressing dipole modes propagating in the DLA structure, thereby mitigating the influence caused by microgap between the two-halves copper jacket.

D. Change the choke gap to meet the requirement for high-power test

After adding power splitters for the full-assembly structure, $S'_{11} = -15.2$ dB and $S'_{21} = -4.96$ dB are achieved. Given that this full-assembly structure will be put into the XBOX system for a high-power test in the near future, the reflection coefficient has to be improved better than $S'_{11} \leq -20$ dB in order to protect our XBOX system. In order to meet this requirement, the choke gap at both sides is changed.

At first, we remove the stainless-steel stick rod which should be inserted into the groove of the outer copper jacket in order to stop it from moving. In this situation, the copper
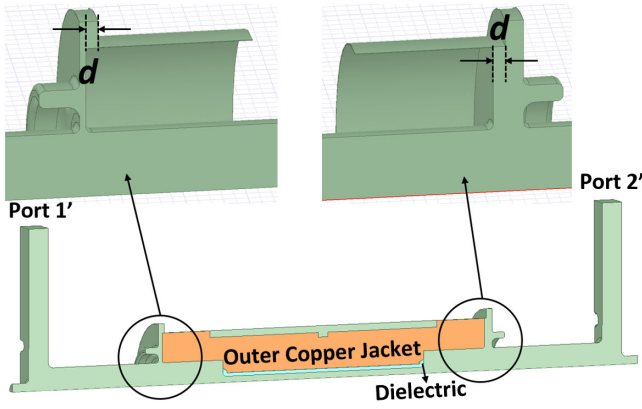
FIG. 25. The choke gap at both sides changes with the moving of the two-halves copper jacket.

jacket enclosing the DLA structure easily slides along the beam axis. If it moves a distance of d, the choke gap at one side increases by d while the choke gap at the other side decreases by d as compared to the original gap of 3 mm, as shown in Fig. 25. It can be seen in Fig. 26 that the measured
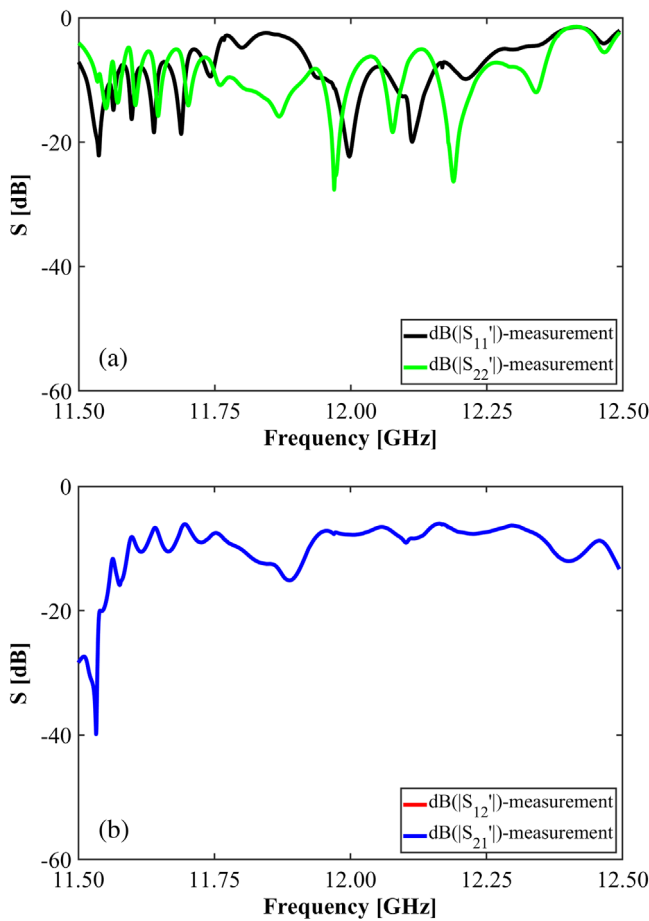
$S'_{11} = -21.4$ dB when $d = 1.0$ mm although measured $S'_{21} = -7.75$ dB is becoming worse. This means that our full-assembly structure meets the requirement of our XBOX system for a high-power test by adjusting the choke gap at both sides. This discrepancy between S'_{11} and S'_{21} may be caused by different fabrication errors on matching sections and different choke gaps at both sides.

V. FABRICATION ERROR ANALYSIS

In this section, fabrication error analysis is performed by adjusting the geometry of the matching section and the two-halves copper jacket to produce an electric field distribution and S parameters which are quite similar to those of rf measurements (see the second row of Table II).

It is found that the amount of electric field magnitude oscillation and the number of periodic peaks in DLA structure are determined by width W_1 of the matching section and the inner radius R_{in} of DLA structure, respectively, in HFSS simulations. When $R_{in} = 2.99$ mm, the simulated electric field has eight periodic peaks at DLA structure, which agrees with both curves in Fig. 20.

FIG. 26. Comparisons between measured (a) S'_{11} and S'_{22}, (b) S'_{12} and S'_{21} for the full-assembly structure with a sliding distance $d = 1.0$ mm.
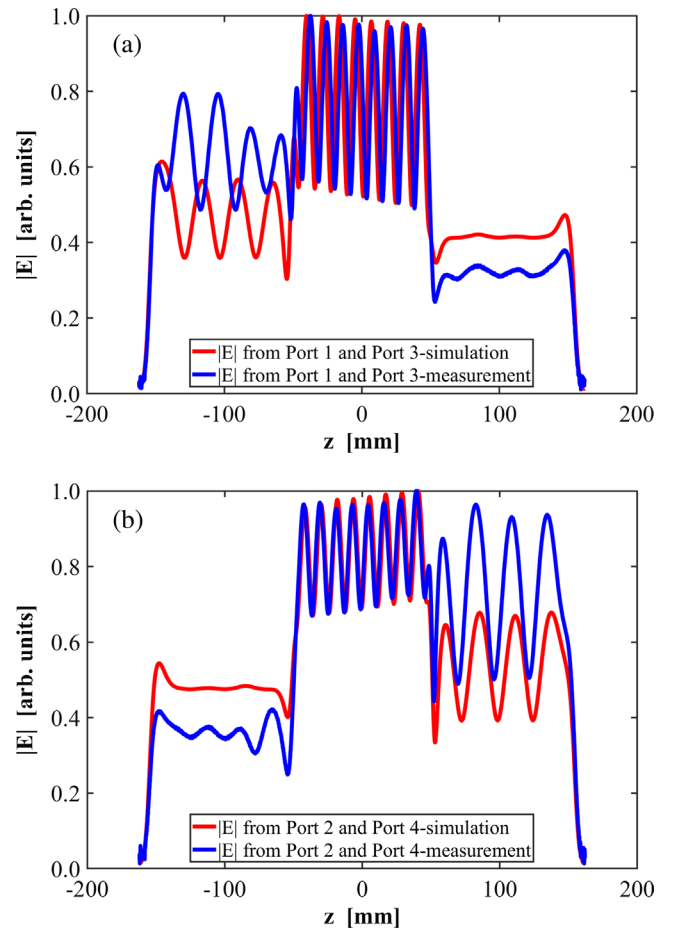

FIG. 27. Comparison between simulated and measured electric field magnitude, for injecting rf power from ports 1 and 3 (a), from ports 2 and 4 (b), respectively.
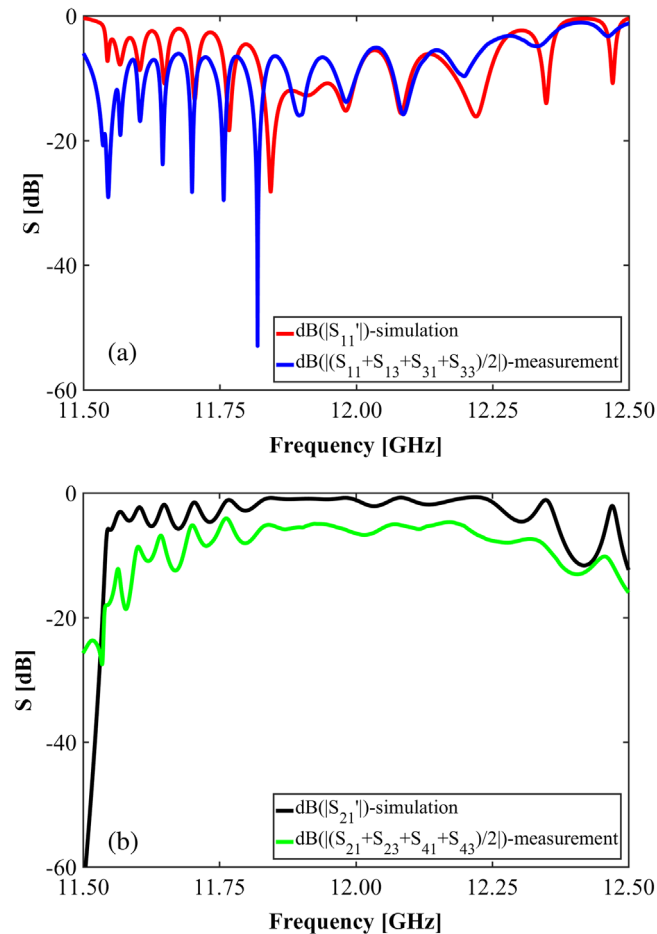
FIG. 28. Comparison between simulated and measured S parameters [(a) S'_{11} and (b) S'_{21}] for the full-assembly structure with $R_{\rm in} = 2.99$ mm, $W_1 = 2.08$ mm at one side and $W_1 = 2.12$ mm at the other side.

When $W_1 = 2.08$ mm for one matching section nearby ports 1 and 3 and $W_1 = 2.12$ mm for the other matching section nearby ports 2 and 4, the simulated electric fields are similar to those of bead-pull measurement, as shown in Fig. 27.

Therefore, the full-structure modeling [see Fig. 18(b)] is modified to have a DLA structure with an inner radius of $R_{\rm in} = 2.99$ mm, one matching section with a geometry of $W_1 = 2.08$ mm at one side and the other matching section with a geometry of $W_1 = 2.12$ mm at the other side. The simulated S parameters for this full-assembly structure are then obtained and compared with the measured S parameters. Figure 28 shows that simulated $S'_{11} = -11.8$ dB is in good agreement with measured $S'_{11} = -11.3$ dB but simulated $S'_{21} = -0.97$ dB is not consistent with measured $S'_{21} = -6.3$ dB at the operating frequency of 11.994 GHz. This means that the fabrication error on the inner radius is estimated to be 0.01 mm which meets the requirement of fabrication accuracy in the subsection of tolerance studies. However, the estimated fabrication error on W_1 for one matching section is 0.045 mm and it is 0.085 mm for the other
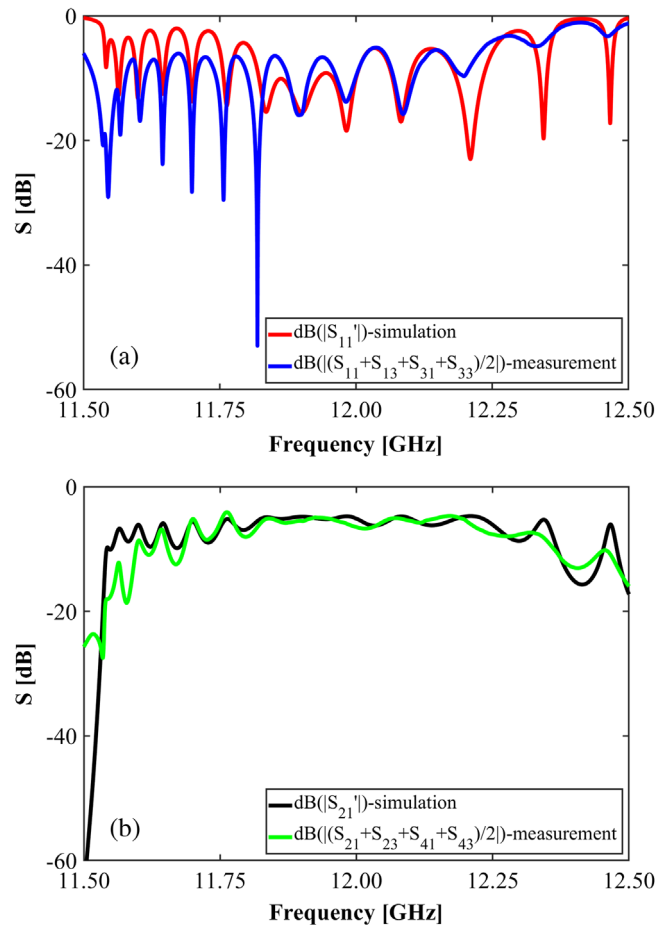

FIG. 29. Comparison between simulated and measured S parameters [(a) S'_{11} and (b) S'_{21}] for the full-assembly structure with $R_{\rm in} = 2.99$ mm, $W_1 = 2.08$ mm at one side and $W_1 = 2.12$ mm at the other side, and an offset of 1.0 mm for the two-halves copper jacket in both horizontal (x axis) and vertical (y axis) directions, a microgap of 1.0 mm with an alignment angle $\beta = 45^{\circ}$ [see Fig. 15(b)].

matching section. Both values of W_1 are out of fabrication tolerances. This may be caused by the absence of measurement during the fabrication process for the dielectric tube. Through carefully machining and measuring the width of matching sections, the values of W_1 can be modified back to the design value of 2.035 mm under tolerances. This will be studied in the next step.

We continue investigating other possible reasons causing the inconsistency between the simulated and measured S'_{21}. Besides the fabrication errors on both $R_{\rm in}$ and W_1, when there is an offset of 1.0 mm for the two-halves copper jacket in both horizontal (x-axis) and vertical (y-axis) directions and a microgap of 1.0 mm with an alignment angle $\beta = 45^{\circ}$ [see Fig. 15(b)], the simulated $S'_{11} = -11.5$ dB and $S'_{21} = -5$ dB dB are obtained at the operating frequency of 11.994 GHz, as shown in Fig. 29. The offset in both directions and the microgap between the two-halves copper jacket cannot be larger than 1.0 mm through the

measurement. In this situation, the simulated electric fields are similar to those of bead-pull measurements. The simulated $S'_{11} = -11.5$ dB has a good agreement with the measured $S'_{11} = -11.3$ dB while there is a difference of 1.3 dB between the simulated S'_{21} and the measured S'_{21} at the operating frequency of 11.994 GHz. This difference may be caused by other fabrication errors, such as misalignment in longitudinal directions and coating quality on the dielectric tube. Further investigations are still required to understand the origin of this difference.

VI. CONCLUSIONS

This paper presented the design, fabrication and low-power rf measurement of an X-band DLA structure at CERN. In order to efficiently couple the rf power from a rectangular waveguide to an X-band DLA structure, the mode converters with choke geometry and the compact dielectric matching sections were carefully designed. Tolerance studies were also carried out for the whole dielectric structure. A full-assembly structure, including the DLA structure connected with two matching sections, TE_{10}-TM_{01} mode converters with choke geometry, was analyzed in detail.

A prototype of the DLA structure with the dielectric matching sections was subsequently built and mechanically assembled with the mode converters for rf measurement. The mode converters were demonstrated to propagate rf power in a normal way. However, a significant discrepancy, due to fabrication errors, was found between measured and simulated S parameters. Geometrical analysis was thus performed to understand the origin of these differences. The fabrication error on width W_1 of the matching sections was found to be the main cause of the large reflection coefficient as a whole. The fabrication errors including the offset for the two-halves copper jacket in both horizontal (x-axis) and vertical (y-axis) directions and the microgap in it resulted in a large attenuation for the transmission of rf power. Through adjusting the choke gap, an overall measured reflection coefficient of $S'_{11} = -21.4$ dB could be reached, which meets the requirement of our XBOX system.

In the next step, the measurement techniques will be introduced during the fabrication processing on the dielectric tube especially on the width of dielectric matching sections. We believe that the dielectric tube with a width of ~ 2.035 mm under the tolerances can be successfully realized through carefully machining and measurement in each step. A new dielectric tube is under fabrication in order to improve the present fabrication processing. Special attention should be also paid to the fabrication and assembly of the two-halves copper jacket with the aim to reduce the offset in both horizontal (x-axis) and vertical (y-axis) directions and the size of microgap.

The current full-assembly structure will be put into the Xbox system for a high-power test. Because of unexpected fabrication errors on the matching sections, the standing-wave field in the whole structure will be very large. This will be an issue to identify the location of a breakdown in a high-power test. It is also foreseen that dielectric rf breakdown [42] and surface resonant multipacting [41–46] would be the primary issues to limit the achievable gradient for DLA structures. Thus, further studies are required to solve these issues. This will be reported in separate publications.

[1] P. Wilson, Z. Farkas, and R. Ruth, Field emission and rf breakdown in high-gradient room-temperature linac structure, Technical Report No. SLAC-PUB-7684, Stanford Linear Accelerator Center, Menlo Park, CA, 1997.

[2] H. Braun, S. Dobert, L. Groening, I. Wilson, and W. Wuensch, Status of CLIC high-gradient studies, in PACS2001, in *Proceedings of the 2001 Particle Accelerator Conference* (IEEE, New York, 2001), Vol. 2, pp. 852–854.

[3] H. H. Braun, S. Dobert, I. Wilson, and W. Wuensch, Frequency and Temperature Dependence of Electrical Breakdown at 21, 30, and 39 GHz, Phys. Rev. Lett. **90,** 224801 (2003).

[4] A. Grudiev, S. Calatroni, and W. Wuensch, New local field quantity describing the high gradient limit of accelerating structures, Phys. Rev. ST Accel. Beams **12,** 102001 (2009).

[5] T. Higo, Progress of X-band accelerating structures, in *Proceedings of the 25th International Linear Accelerator Conference, LINAC2010, Tsukuba, Japan* (JACoW, Geneva, 2010), pp. 1038–1042.

[6] W. Gai, P. Schoessow, B. Cole, R. Konecny, J. Norem, J. Rosenzweig, and J. Simpson, Experimental Demonstration of Wakefield Effects in Dielectric Structures, Phys. Rev. Lett. **61,** 2756 (1988).

[7] I. Blumenfeld, C. Clayton, F. J. Decker *et al.*, Energy doubling of 42 GeV electrons in a meter-scale plasma wakefield accelerator, Nature (London) **445,** 741 (2007).

[8] E. Esarey, C. Schroeder, and W. Leemans, Physics of laser-driven plasma-based electron accelerators, Rev. Mod. Phys. **81,** 1229 (2009).

[9] R. J. England, R. J. Noble, K. Bane, D. H. Dowell, C.-K. Ng, J. E. Spencer, S. Tantawi, Z. Wu, R. L. Byer, E. Peralta *et al.*, Dielectric laser accelerators, Rev. Mod. Phys. **86,** 1337 (2014).

[10] E. Adli, A. Ahuja, O. Apsimon *et al.* Acceleration of electrons in the plasma wakefield of a proton bunch, Nature (London) **561,** 363 (2018).

[11] Y. Wei, Dielectric structure development, in *International Workshop on Breakdown Science and High Gradient Technology (HG2019), Chamonix, France, 2019*, https://indico.cern.ch/event/766929/contributions/3439358/.

[12] W. Gai and C. Ho, Modeling of the transverse mode suppressor for dielectric wakefield accelerator, J. Appl. Phys. **70**, 3955 (1991).

[13] E. Chojnacki, W. Gai, C. Ho, R. Konecny, S. Mtingwa, J. Norem, M. Rosing, P. Schoessow, and J. Simpson, Measurement of deflection-mode damping in an accelerating structure, J. Appl. Phys. **69**, 6257 (1991).

[14] W. K. H. Panofsky and M. Bander, Asymptotic theory of beam breakup in linear accelerators, Rev. Sci. Instrum. **39**, 206 (1968).

[15] S. Frankel, TM0,1 mode in circular waveguides with two coaxial dielectrics, J. Appl. Phys. **18**, 650 (1947).

[16] G. G. Bruck and E. R. Wicher, Slow transverse magnetic waves in cylindrical guides, J. Appl. Phys. **18**, 766 (1947).

[17] A. A. Oliner, Remarks on slow waves in cylindrical guides, J. Appl. Phys. **19**, 109 (1948).

[18] R. B. R.-Shersby-Harvie, A proposed new form of dielectric-loaded waveguide for linear electron accelerators, Nature (London) **162**, 890 (1948).

[19] G. I. Cohn and G. T. Flesher, Design construction and initial operation of a continuous dielectric loaded linear accelerator, Illinois Institute of Technology Report No. 2 Electronics Research Laboratories, 1952.

[20] R. B. R.-Shersby-Harvie, L. B. Mullett, W. Walkinshaw, J. S. Bell, and B. G. Loach, A theoretical and experimental investigation of anisotropic-dielectric-loaded linear electron accelerators, in, *Proceedings of the IEE—Part B: Radio and Electronic Engineering* (1957), No. 15, Vol. 104, pp. 273–290, 10.1049/pi-b-1.1957.0153.

[21] G. B. Walker and E. L. Lewis, Vacuum breakdown in dielectric-loaded waveguides, Nature (London) **181**, 38 (1958).

[22] R. A. Woode, E. N. Ivanov, M. E. Tobar, and D. G. Blair, Measurement of dielectric loss tangent of alumina at microwave frequencies and room temperature, Electron. Lett. **30**, 2120 (1994).

[23] N. M. Alford and S. J. Penn, Sintered alumina with low dielectric loss, J. Appl. Phys. **80**, 5895 (1996).

[24] C. L. Huang, J. J. Wang, and C. Y. Huang, Microwave dielectric properties of sintered alumina using nanoscaled powders of α alumina and TiO2, J. Am. Ceram. Soc. **90**, 1487 (2007).

[25] A. Templeton, X. Wang, S. J. Penn, S. J. Webb, L. F. Cohen, and N. M. Alford, Microwave dielectric loss of titanium oxide, J. Am. Ceram. Soc. **83**, 95 (2000).

[26] J. D. Breeze, X. Aupi, and N. M. Alford, Ultralow loss polycrystalline alumina, Appl. Phys. Lett. **81**, 5021 (2002).

[27] W. Gai, Advanced accelerating structures and their interaction with electron beams, AIP Conf. Proc. **1086**, 3 (2009).

[28] A. Kanareykin, New advanced dielectric materials for accelerator applications, AIP Conf. Proc. **1299**, 286 (2010).

[29] P. Schoessow, A. Kanareykin, and R. Gat, CVD diamond dielectric accelerating structures, *AIP Conf. Proc.* 1086, 398 (2009).

[30] C. Jing, A. Kanareykin, J. G. Power, M. Conde, Z. Yusof, P. Schoessow, and W. Gai, Observation of Enhanced Transformer Ratio in Collinear Wakefield Acceleration, Phys. Rev. Lett. **98**, 144801 (2007).

[31] C. Jing, Dielectric wakefield accelerators, Rev. Accel. Sci. Techol. **09**, 127 (2016).

[32] P. Zou, L. Xiao, X. Sun, W. Gai, and T. Wong, Hybrid dielectric and iris-loaded periodic accelerating structure, J. Appl. Phys. **90**, 2017 (2001).

[33] C. Jing, A. Kanareykin, S. Kazakov, W. Liu, E. Nenasheva, P. Schoessow, and W. Gai, Development of a dual-layered dielectric-loaded accelerating structure, Nucl. Instrum. Methods Phys. Res., Sect. A **594**, 132 (2008).

[34] C. Jing, W. M. Liu, W. Gai, J. G. Power, and T. Wong, Mode analysis of a multilayered dielectric-loaded accelerating structure, Nucl. Instrum. Methods Phys. Res., Sect. A **539**, 445 (2005).

[35] A. V. Smirnov, S. Boucher, S. Kutsaev, J. Hartzell, and E. Savin, Multicell disk-and-ring tapered structure for compact rf linacs, Nucl. Instrum. Methods Phys. Res., Sect. A **830**, 294 (2016).

[36] J. Shao, C. Jing, J. Power, M. Conde, and D. Doran, Study of a dielectric disk structure for short pulse two-beam acceleration, in *Proceedings of the 9th International Particle Accelerator Conference, IPAC2018, Vancouver, BC, Canada* (JACoW, Geneva, 2018), pp. 1539–1541.

[37] D. Satoh, M. Yoshida, and N. Hayashizaki, Dielectric assist accelerating structure, Phys. Rev. Accel. Beams **19**, 011302 (2016).

[38] D. Satoh, M. Yoshida, and N. Hayashizaki, Fabrication and cold test of dielectric assist accelerating structure, Phys. Rev. Accel. Beams **20**, 091302 (2017).

[39] S. Mori, M. Yoshida, and D. Satoh, Multipactor suppression in dielectric-assist accelerating structures via diamondlike carbon coatings, Phys. Rev. Accel. Beams **24**, 022001 (2021).

[40] Y. Wei and A. Grudiev, Investigations into *X*-band dielectric assist accelerating structures for future linear accelerators, IEEE Trans. Nucl. Sci. **68**, 1062 (2021).

[41] J. G. Power, W. Gai, S. H. Gold, A. K. Kinkead, R. Konecny, C. Jing, W. Liu, and Z. Yusof, Observation of Multipactor in an Alumina-Based Dielectric-Loaded Accelerating Structure, Phys. Rev. Lett. **92**, 164801 (2004).

[42] C. Jing, W. Gai, J. G. Power, R. Konecny, S. H. Gold, W. Liu, and A. K. Kinkead, High-power rf tests on *X*-band dielectric-loaded accelerating structures, IEEE Trans. Plasma Sci. **33**, 1155 (2005).

[43] C. Jing, W. Gai, J. G. Power, R. Konecny, W. Liu, S. H. Gold, A. K. Kinkead, S. G. Tantawi, V. Dolgashev, and A. Kanareykin, Progress toward externally powered x-band dielectric-loaded accelerating structures, IEEE Trans. Plasma Sci. **38**, 1354 (2010).

[44] C. Chang, J. Verboncoeur, S. Tantawi, and C. Jing, The effects of magnetic field on single-surfaceresonant multipactor, J. Appl. Phys. **110**, 063304 (2011).

[45] C. Jing, C. Chang, S. H. Gold, R. Konecny, S. Antipov, P. Schoessow, A. Kanareykin, and W. Gai, Observation of multipactor suppression in a dielectric-loaded accelerating structure using an applied axial magnetic field, Appl. Phys. Lett. **103**, 213503 (2013).

[46] C. Jing, S. H. Gold, R. Fischer, and W. Gai, Complete multipactor suppression in an *X*-band dielectric-loaded accelerating structure, Appl. Phys. Lett. **108,** 193501 (2016).

[47] M. C. Thompson, H. Badakov, A. M. Cook, J. B. Rosenzweig, R. Tikhoplav, G. Travish, I. Blumenfeld, M. J. Hogan, R. Ischebeck, N. Kirby, R. Siemann, D. Walz, P. Muggli, A. Scott, and R. B. Yoder, Breakdown Limits on Gigavolt-per-Meter Electron-Beam-Driven Wakefields in Dielectric Structures, Phys. Rev. Lett. **100,** 214801 (2008).

[48] P. Zou, W. Gai, R. Konecny, X. Sun, T. Wong, and A. Kanareykin, Construction and testing of an 11.4 GHz dielectric structure based traveling wave accelerator, Rev. Sci. Instrum. **71,** 2301 (2000).

[49] J. G. Power, W. Gai, C. Jing, R. Konecny, S. H. Gold, and A. K. Kinkead, High power testing of ANL *X*-band dielectric-loaded accelerating structures, AIP Conf. Proc. **647,** 156 (2002).

[50] W. Liu and W. Gai, Design of dielectric accelerator using TE-TM mode converter, AIP Conf. Proc. **647,** 469 (2002).

[51] W. Liu, C. Jing, W. Gai, R. Konecny, and J. G. Power, New rf design for 11.4 GHz dielectric loaded accelerator, in *Proceedings of the 2003 Particle Accelerator Conference, Portland, Oregon* (IEEE, Piscataway, NJ, 2003), pp. 1810–1812.

[52] K. A. Thompson *et al.*, Design and simulation of accelerating structures for future linear colliders, Part. Accel. **47,** 65 (1994), https://slac.stanford.edu/pubs/slacpubs/6000/slac-pub-6032.pdf.

[53] R. H. Miller *et al.*, A damped detuned structure for the next linear collider, Report No. SLAC-PUB-7288, 1996.

[54] C. Adolphsen *et al.*, Zeroth-order design report for the next linear collider, SLAC Report No. 474, 1996.

[55] N. Akasaka *et al.*, JLC Design Study, Report No. KEK-Report-97-1, 1997.

[56] Report No. SLAC-R-606, International Linear Collider, Technical Review Committee, Second Report 2003.

[57] S. Dobert, Gradient limitations for high-frequency accelerators, in *Proceedings of LINAC 2004, Lübeck, Germany* (JACoW, Geneva, 2004), pp. 513–517.

[58] S. Dobert, C. Adolphsen, G. Bowden *et al.*, High gradient performance of NLC/GLC *X*-band accelerating structures, in *Proceedings of the 21st Particle Accelerator Conference, Knoxville, TN, 2005* (IEEE, Piscataway, NJ, 2005), pp. 372–374.

[59] C. Adolphsen, Advances in normal conducting accelerator technology from the *X*-band linear collider program, in *Proceedings of the 21st Particle Accelerator Conference, Knoxville, TN, 2005* (Ref. [58]), pp. 204–208.

[60] G. Aarons *et al.*, International Linear Collider, Reference Design Report, 2007, http://ilcdoc.linearcollider.org/record/6321/files/ILC_RDR_Volume_3-Accelerator.pdf.

[61] M. Aicheler *et al.*, A multi-TeV linear collider based on CLIC technology: CLIC conceptual design report, 2012.

[62] T. Higo, Y. Higashi, S. Matsumoto, K. Yokoyama, and J. W. Wang, Advances in *X*-band TW accelerator structures operating in the 100 MV/m regime, in *Proceedings of 1st International Particle Accelerator Conference (IPAC 10), Kyoto, Japan* (JACoW, Geneva, 2010), pp. 3702–3704.

[63] T. Higo, T. Abe, Y. Arakida *et al.*, Comparison of high gradient performance in varying cavity geometries, in *Proceedings of 4th International Particle Accelerator Conference (IPAC 13), Shanghai, China* (JACoW, Geneva, 2013), pp. 2741–2743.

[64] A. Grudiev and W. Wuensch, A newly designed and optimized CLIC main linac accelerating structure, in *Proceedings of the 19th International Linear Accelerator Conference, LINAC2004, Lübeck, Germany* (JACoW, Geneva, 2004), pp. 779–781.

[65] R. Zennaro, A. Grudiev, G. Riddone, A. Samoshkin, W. Wuensch, S. Tantawi, J. W. Wang, and T. Higo, Design and fabrication of CLIC test structures, in *Proceedings of the 23rd International Linear Accelerator Conference, LINAC2008, Victoria, BC, Canada* (JACoW, Geneva, 2008), pp. 533–535.

[66] A. Grudiev and W. Wuensch, Design of the CLIC main linac accelerating structure for CLIC Conceptual Design Report, in *Proceedings of the 25th International Linear Accelerator Conference, LINAC2010, Tsukuba, Japan* (Ref. [5]).

[67] H. Zha, A. Grudiev, and V. Dolgashev, RF design of the CLIC structure prototype optimized for manufacturing from two halves, in *Proceedings of the 6th International Particle Accelerator Conference, IPAC2015, Richmond, VA, USA* (JACoW, Geneva, 2015), pp. 2147–2149.

[68] H. Zha and A. Grudiev, Design and optimization of Compact Linear Collider main linac accelerating structure, Phys. Rev. Accel. Beams **19,** 111003 (2016).

[69] H. Zha and A. Grudiev, Design of the Compact Linear Collider main linac accelerating structure made from two halves, Phys. Rev. Accel. Beams **20,** 042001 (2017).

[70] K. L. Bane, T. L. Barklow, M. Breidenbach *et al.*, An advanced NCRF linac concept for a high energy e^+e^- linear collider, arXiv:1807.10195.

[71] S. Tantawi, M. Nasr, Z. Li, C. Limborg, and P. Borchard, Design and demonstration of a distributed-coupling linear accelerator structure, Phys. Rev. Accel. Beams **23,** 092001 (2020).

[72] G. D'Auria, *X*-band technology applications at FERMI@Elettra FEL project, Nucl. Instrum. Methods Phys. Res., Sect. A **657,** 150 (2011).

[73] G. D'Auria, S. Di Mitri, C. Serpico *et al.*, *X*-band technology for FEL sources, in *Proceedings of the 29th International Linear Accelerator Conference, LINAC2014, Geneva, Switzerland* (CERN, Geneva, Switzerland, 2014), pp. 101–104.

[74] A. Aksoy, Ö. Yavaş, D. Schulte *et al.*, Conceptual design of an X-FEL facility using CLIC *X*-band accelerating structure, in *Proceedings of the 5th International Particle Accelerator Conference, IPAC2014, Dresden, Germany* (JACoW, Geneva, 2014), pp. 2914–2917.

[75] A. Aksoy, A. Latina, J. Pfingstner, D. Schulte, and Z. Nergiz, Design optimization of an *X*-band based FEL, in *Proceedings of the 7th International Particle Accelerator Conference, IPAC2016, Busan, Korea* (JACoW, Geneva, 2016), pp. 793–796.

[76] J. B. Rosenzweig, N. Majernik, R. R. Robles *et al.*, An ultracompact x-ray free-electron laser, New J. Phys. **22,** 093067 (2020).

[77] K. Dobashi, M. Uesaka, A. Fukasawa *et al.*, *X*-band rf gun and linac for medical Compton scattering x-ray source, *AIP Conf. Proc.* 737, 684 (2004).

[78] W. Wuensch, Applications of *X*-band and high-gradient technology, *CLIC Project Meeting, 2019*, https://indico. cern.ch/event/862915/contributions/3636126/attachments/ 1956781/3250679/CLIC_project_meeting_ww.pdf.

[79] Y. Lee, S. Kim, G. Kim *et al.*, Medical *X*-band linear accelerator for high-precision radiotherapy, Med. Phys. **48,** 5327 (2021).

[80] https://www.qwed.com.pl/resonators_te01.html.

[81] HFSS, https://www.ansys.com.

[82] Y. Wei, A. Grudiev, B. Freemire, and C. Jing, A compact, low field, broadband matching section for externally powered *X*-band dielectric-loaded ac-celerating structures, arXiv:2008.09203.

[83] https://www.insaco.com/.

[84] I. Syratchev, Mode launcher as an alternative approach to the cavity-based rf coupler of periodic structures, Report No. CERN-OPEN-2002-005, 2002.

[85] N. Catalan-Lasheras, A. Degiovanni, S. Doebert, W. Farabolini, J. Kovermann, G. McMonagle, S. Rey, I. Syratchev, L. Timeo, W. Wuensch, B. Woolley, and J. Tagg, Experience operating an *X*-band high-power test stand at CERN, in *Proceedings of the 5th International Particle Accelerator Conference, IPAC2014, Dresden, Germany* (Ref. [74]), pp. 2288–2290.

[86] A. V. Edwards, N. Catalan Lasheras, S. Gonzalez Anton, G. Mcmonagle, S. Pitman, V. del Pozo Romano, B. Woolley, and A. Dexter, Connection of 12 GHz high power rf from the XBOX1 high gradient test stand to the CLEAR electron linac, in *Proceedings of the 10th International Particle Accelerator Conference, IPAC2019, Melbourne, Australia* (JACoW, Geneva, 2019), pp. 2960– 2963.

[87] L. C. Maier Jr. and J. C. Slater, Field strength measurements in resonant cavities, J. Appl. Phys. **23,** 68 (1952).

[88] J. Shi, A. Grudiev, and W. Wuensch, Tuning of *X*-band traveling-wave accelerating structures, Nucl. Instrum. Methods Phys. Res., Sect. A **704,** 14 (2013).